PAPER

Very high thermoelectric power factor near magic angle in twisted bilayer graphene

To cite this article: Adithya Kommini and Zlatan Aksamija 2021 2D Mater. 8 045022

View the article online for updates and enhancements.



ICE

iceoxford.com

High cooling power, low vibration cryostats with fast sample turnaround times.

Range of 3K, 1.5K, 300mK and 15mK systems for 2D Materials Research.

2D Materials



12 April 2021

REVISED 4 June 2021

ACCEPTED FOR PUBLICATION 19 July 2021

PUBLISHED 20 August 2021

PAPER

Very high thermoelectric power factor near magic angle in twisted bilayer graphene

Adithya Kommini and Zlatan Aksamija* 🗓

University of Massachusetts Amherst, Amherst, MA 01003, United States of America

Author to whom any correspondence should be addressed.

E-mail: zlatana@engin.umass.edu

Keywords: thermoelectric, graphene, twisted bilayer

Abstract

Recent research on twisted bilayer graphene (TBG) uncovered that its twist-angle-dependent electronic structure leads to a host of unique properties, such as superconductivity, correlated insulating states, and magnetism. The flat bands that emerge at low twist angles in TBG result in sharp features in the electronic density of states, affecting transport. Here we show that they lead to superior and tuneable thermoelectric (TE) performance. Combining an iterative Boltzmann transport equation solver and electronic structure from an exact continuum model, we calculate TE transport properties of TBG at different twist angles, carrier densities, and temperatures. Our simulations show the room-temperature TE power factor (PF) in TBG reaches 40 mW m $^{-1}$ K $^{-2}$, significantly higher than single-layer graphene and among the highest reported to date. The peak PF is observed near the magic angle, at a twist angle of \approx 1.3°, and near complete band filling. We elucidate that its dependence is driven by two opposing forces: the band gap between the flat and remote bands suppresses bipolar transport and improves the Seebeck coefficient but the gap decreases with twist angle; on the other hand, the Fermi velocity, which impacts conductivity, is smallest at the magic angle and rises with twist angle. We observed a further increase in the PF of TBG with decreasing temperature. The strong TE performance, along with the ability to fine-tune transport using twist angle, makes TBG an interesting candidate for future research and applications in energy conversion and thermal sensing and management.

Ever-increasing demand for sustainable energy resources amplifies the need to improve the efficiency of existing power generation techniques and develop novel approaches across a broad swath of size scales. Waste-heat recovery through solid-state thermoelectric (TE) devices is one such approach that can contribute to robust small-scale energy scavenging and thermal management. Their widespread adoption may require new materials with high TE performance, typically measured by the dimensionless figure-of-merit ZT [1]. ZT is proportional to the power factor (PF), given by the product $S^2 \sigma$ of electrical conductivity σ and the Seebeck coefficient Ssquared. There is a well-established trade-off between σ , which increases with carrier concentration, and S, which decreases with it. Band-engineering techniques [2–4] have been pursued to decouple this dependency and improve the PF by introducing sharp features in the electronic density-of-state (DOS), whose large slope benefits S. A complementary approach

is by employing low-dimensional materials, such as graphene, that naturally possess a suitable DOS. Single-layer graphene (SLG) on hexagonal boron nitride (hBN) substrates has achieved the highest known room-temperature PF of 36 mW m⁻¹K⁻² [5]. Beyond power generation applications, high-PF materials like graphene can enhance active cooling, which is vital for thermal management in electronic devices [6]. Furthermore, graphene thermocouples exhibit the highest reported sensitivity [7], which can be used in reliable temperature sensors.

Recent studies showed that absence of Fermi velocity at certain magic angles in twisted bilayer graphene (TBG) results in robust superconductivity [8, 9] at low temperatures. The theoretically predicted [10, 11] and observed [12] flat bands near magic angles contribute to superconducting states depending on the carrier density and twist angle. These remarkably flat bands with strongly correlated states also exhibit correlated insulator behavior [13]

2D Mater. **8** (2021) 045022 A Kommini and Z Aksamija

at nearly all integer fillings of fourfold degenerate flat conduction and valence bands [14]. The flat bands [12] greatly enhance sharp features in the carrier DOS [10] while saddle points lead to closely spaced van Hove singularities near the Fermi level [15], which, if coupled with good carrier conductivity, are highly desirable for TE applications. This combination of features in the DOS, in addition to the secondary bandgap between the lowest and second subbands in TBG, creates a narrow transport distribution function (TDF) [16]. Then states bunched around sharp features in the DOS translate into improved Seebeck coefficient and maximize the PF [17, 18]. The highly tunable band structure of TBG offers a new lever of control and a novel avenue to further decouple Seebeck and conductivity to achieve unprecedented PFs. Mahapatra et al studied the twist-angle dependence of thermoelectricity in TBG junctions [19] and found it to be highly sensitive to electronic structure. In the cross-plane direction, thermopower is driven by interlayer phonon drag for angles above 6° while the electron diffusion component was recovered below 6° [20]. However, little is yet known about the in-plane TE performance of TBG and its dependence on twist angle except at very low temperatures [21].

Here we study the impact of the unique band structure and sharp features in the DOS on carrier transport and TE properties of TBG. We numerically solve the Boltzmann transport equation (BTE) using band structure obtained from a recently published exact continuum model coupled with a fullband variant of Rode's iterative method to model the carrier transport in TBG. Our model shows TBG has an exceptionally high PF near, but not coinciding with, the magic twist angle. We explain this behavior via the trade-off between bands flattening on the one hand, which benefits the Seebeck, and Fermi velocity dropping, which lowers conductivity. The peak room-temperature PF of 40 mW m⁻¹ K⁻² is among the highest ever reported and significantly higher than in SLG. Compared to SLG, the PF in TBG is driven by a more favorable trade-off between conductivity and Seebeck, which reaches up to 150 μ V K⁻¹. We observe further increases in the PF when the temperature is lowered to 200 and 100 K, consistent with the presence of a small band gap.

We have implemented a self-consistent Jacobi iterative scheme to solve the linearized BTE and include the full band structure as input [22, 23]. Our approach to solving the BTE is based on Rode's method [24] to incorporate inelastic scattering, particularly the in-scattering terms in the collision integral. This is important in a Dirac material like graphene where transport is predominantly bipolar and significantly affected by inelastic scattering [25]. The carrier probability can be written as a sum of the equilibrium component (determined by Fermi–Dirac statistics, $f_0(k)$) and a small perturbation (g(k)) in the direction of the applied field, $f(k) = f_0(k) + g(k)$.

Using the standard Boltzmann form of the collision operator, the perturbation to carrier distribution is calculated by iterating

$$g_{i+1}(k) = (I_i(k) + eF \nabla_k f_0 - \nu(k) \cdot \nabla_r f_0) / S_o(k),$$
 (1)

where the in-scattering integral is

$$I_{i}(k) = \Lambda \int \left[N(\omega_{ph}) - f(k) + \frac{1}{2} \mp \frac{1}{2} \right] g_{i}(k') \, \delta(E(k))$$
$$\pm \hbar \omega_{ph} - E(k') dk', \tag{2}$$

 S_o is the total scattering rate (inverse of relaxation time) and F is the applied electric field. The term $eF\nabla_k f_0$ can be expanded to get $(e/\hbar)F\cdot v(k)\partial f_0/\partial E$ with $v(k)=1/\hbar\nabla_k E(k)$ being the carrier group velocity while the $\partial f_0/\partial E$ is the Fermi window that determines the range of energies contributing to transport.

In strongly correlated systems or 'strange metals', resistivity scales linearly with temperature, similar to what was observed in TBG [26, 27]. In these materials, quantum fluctuations are proposed to be the dominant scattering mechanism that results in T-linear behavior [28, 29]. However, the T-linear resistivity is observed at a broad range of twist angles in TBG, independent of the correlated phases at magic angles [30]. This indicates a unified scattering mechanism controls carrier transport. Phonons have been identified as that mechanism [31] and inelastic phonon scattering was shown to dominate carrier transport above the superconducting critical temperature T_c [32]. Hence this study focuses on simulating phonon-limited carrier transport at and above 100 K, well in excess of the Bloch-Grüneisen temperature [33] and in the range of typical energy and sensing applications. Lower temperatures also result in hydrodynamic transport [34] and an enhanced contribution from phonon drag [35], which are beyond the scope of our model. The scattering processes included here are acoustic phonon scattering (Γ_{ac})

$$\Gamma_{ac}(E) = \frac{2\pi D_{ac}^2 k_B T}{\hbar \rho v_{ac}^2} \int \delta(E - E(k')) dk'$$

$$= \frac{2\pi D_{ac}^2 k_B T}{\hbar \rho v_{ac}^2} D(E), \tag{3}$$

where D(E) is the DOS, and inelastic optical phonon scattering (Γ_{op})

$$\Gamma_{op}(k) = \frac{\pi D_{op}^2}{\rho \omega_{op}} \int \left[N(\omega_{op}) - f(k') + \frac{1}{2} \mp \frac{1}{2} \right] \delta(E(k))$$

$$\pm \hbar \omega_{op} - E(k') dk', \tag{4}$$

where the top sign represents absorption processes and bottom emission processes. Here, D_{ac} is the acoustic deformation potential, D_{op} is the optical deformation potential, ρ is the mass density, ν_{ac} is the sound velocity of acoustic phonon modes, ω_{op} is the optical phonon frequency, $N(\omega_{op})$ is phonon

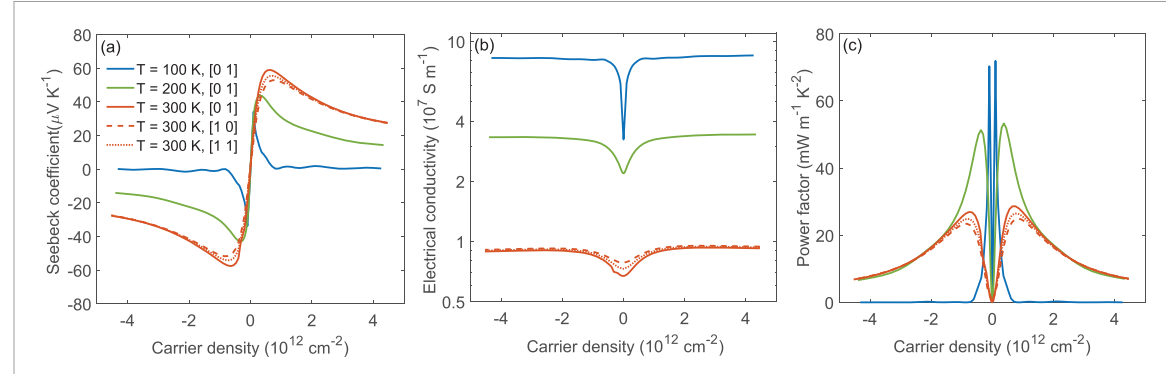


Figure 1. TE properties of SLG (a) Seebeck coefficient, (b) electrical conductivity, and (c) PF calculated at different temperatures. The peak in S is observed when applied electric field in [0 1] direction at T = 300 K. This translates to higher PF in [0 1] direction. S_{eff} decreases with decreasing temperature while σ_{eff} increases.

distribution function and f(k') is the carrier probability distribution of the final state. In equation (4), the constants in front of the integral together make up the scattering-dependent pre-factor Λ used in equation (2) [22].

The Brillouin zone integrals are evaluated numerically using a 2D version of spherical averaging (SAVE) method [36]. In SAVE, we linearly extrapolate the band structure inside a small circle of radius R_s around each point k' in the discretization to compute the length of the constant-energy contour, then sum all the contributions with a weight of $\Lambda(k')g_i(k')$. Once the Jacobi iteration reaches convergence, as measured by the relative error between successive iterations, the converged g(k) is used to calculate TDF as

$$\sigma(E) = \frac{1}{\Omega(2\pi)^2 F} \int \nu(k) g(k) \delta(E - E(k)) d^2k \quad (5)$$

where Ω is the volume of the first Brillouin zone. The S and σ of each carrier type are calculated from the TDF as

$$\sigma = \int \sigma(E)dE,\tag{6}$$

$$S = -\frac{1}{eT} \frac{\int \sigma(E)(E - E_f)dE}{\int \sigma(E)dE}$$
 (7)

with E_f being Fermi energy level and T the temperature of the material. Due to the bipolar nature of the transport in TBG, the effective Seebeck coefficient (S_{eff}) is calculated by combining the electron (S_n) and hole Seebeck coefficient (S_p) over their respective conductivities $(\sigma_n \text{ and } \sigma_p)$, $S_{eff} = (S_n \sigma_n + S_p \sigma_p)/(\sigma_n + \sigma_p)$. The total carrier conductivity is the sum of electron and hole conductivity, $\sigma_{eff} = \sigma_n + \sigma_p$.

In order to validate our model, we first calculated TE properties of SLG, using electronic band structure obtained from first principles in our previous work [37]. Scattering rates are calculated using equations (3) and (4) with $D_{ac} = 3$ eV, $D_{op}^{\Gamma} = 100$ eV nm⁻¹ at Γ -point, and $D_{op}^{K} = 200$ eV nm⁻¹ at Γ -point. The deformation potentials are taken from [38] and

adjusted to match the Seebeck coefficient [39] and maximum PF [25] from the literature. The inelastic optical phonon processes are calculated at optical phonon energies of $\omega_{op}^{\Gamma}=1589~{\rm cm}^{-1}=0.197~{\rm eV}$ at Γ -point and $\omega_{op}^{K}=1197~{\rm cm}^{-1}=0.148~{\rm eV}$ at K-point taken from [40]. Figure 1(a) shows the S_{eff} calculated for SLG at different temperatures by varying the carrier densities using Rode's method. Our S_{eff} and σ_{eff} (figure 1) for SLG are in agreement with measurements on hBN-encapsulated samples [25, 41]. However, scattering from charged impurities in the environment can impact transport, lowering conductivity but raising the Seebeck [42]. We neglect impurities here as their location and concentration varies from sample to sample depending on preparation conditions. A peak PF of 29 mW m⁻¹ K⁻² is observed in SLG for electrons and 30 mW m⁻¹ K² for holes at 300 K in figure 1(c) when electric field is applied in [0 1] direction, in good agreement with measurements [39, 41], confirming the need to include the contribution from inelastic processes [43].

Next, our model was used for TBG to calculate the TE properties at different twist angles. The twistangle-resolved band structure of TBG used in this study is obtained from an openly available exact continuum model developed in reference [44, 45]. The exact continuum model is based on $k \cdot p$ perturbation theory, combining the computational efficiency of tight-binding Hamiltonians with the twist-angle control offered by continuum models. In figures 2(a) and (b), we plot two representative examples of electronic band structures used in this study at twist angles θ = 1.01° and θ = 1.35°, respectively, showing the flat bands near magic angle; the low energy bands open up with increasing twist angle (figure 2(b)) and eventually recover the Dirac cone at the K-point. The secondary band gap $(E_g \text{ shown in figure } 2(b))$ between the first and second subbands of electrons and holes influences carrier transport, especially at half-filling where the material exhibits correlated insulator behavior [46].

Due to the presence of flat bands and gaps, the DOS of TBG has sharp features that are affected

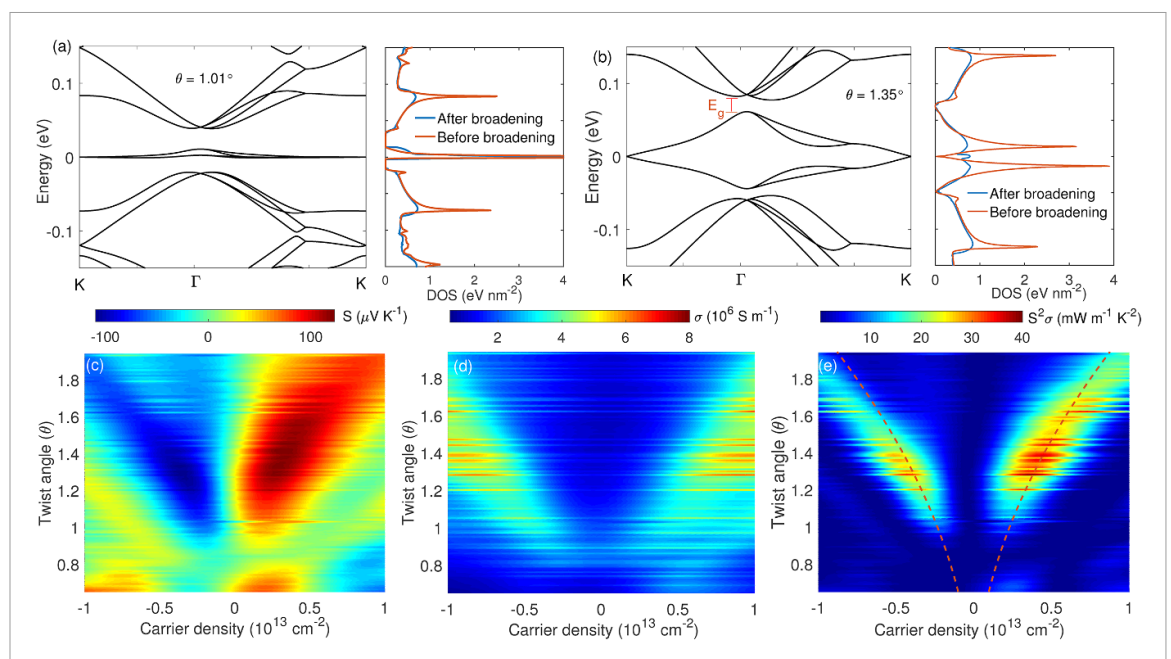


Figure 2. Band structure and density of states (DOS) of TBG at different twist angles (a) 1.01° and (b) 1.35° . Room temperature (c) Seebeck coefficient(S), (d) electrical conductivity (σ), and (e) PF of TBG at different twist angles. The peak in PF is observed at a twist angle of 1.33° . At this twist angle, we observe a maximum in S, which results in the highest PF. The dotted lines represent $\pm n_s$, the carrier density required to completely fill the lowest moiré subband.

by interactions with the lattice at temperatures of interest here. Collision broadening [47, 48] from carrier scattering with phonons is implemented in this study by relating the scattering rate to the imaginary part of self energy $\Gamma(k) = -(2/\hbar)\Im\Sigma(k)$ and replacing the energy-conserving δ in equations (2)–4 with a Lorentzian spectral function $(1/\pi)\Gamma(k)/[(E(k)\pm$ $\hbar\omega_{ph} - E(k')^2 + \Gamma(k)^2$ [49, 50]. The DOS calculated after applying collision broadening is shown in figures 2(a) and (b) and compared with the unbroadened DOS to show that broadening partially smooths out some of the sharp features in the DOS. Acoustic phonon scattering in TBG is calculated with an acoustic deformation potential of $D_{ac} = 9$ eV. This is in line with literature values that suggest D_{ac} of TBG is three times higher than the value observed in SLG [30, 51, 52]. $D_{op}^{\Gamma}=10$ eV nm $^{-1}$ with optical phonon energy of 0.150 meV (1213 cm $^{-1}$) at Γ -point [40] and $D_{op}^{K} = 20 \text{ eV nm}^{-1}$ [51] with optical phonon energies of 0.148 meV (1197 cm⁻¹) at Kpoint are used to calculate the inelastic phonon scattering rates.

Applying our model, we calculated S_{eff} , σ_{eff} , and PF in the [0 1] crystallographic direction at $T=300~\rm K$ and plotted them in figures 2(c)–(e) with respect to twist angle and carrier density. Our calculations show that at room temperature, holes have S_{eff} of 122 $\mu V~\rm K^{-1}$, which is slightly higher than 107 $\mu V~\rm K^{-1}$ obtained for electrons in figure 3(a). The peak in S_{eff} observed at a twist angle of $\theta=1.33^{\circ}$ with a carrier density of $3\times 10^{12}~\rm cm^{-2}$ in holes and $4\times 10^{12}~\rm cm^{-2}$ in electrons. The peak in S_{eff} translates to the peak in PF as seen in figure 2(c) being significantly higher than SLG. In figure 3(a), S_{eff} observed at $\theta=1.33^{\circ}$ is

compared with S_{eff} near magic angle ($\theta = 1.08^{\circ}$) and $\theta = 1.50^{\circ}$. Comparing S_{eff} at these twist-angles with their corresponding DOS (figure 3(c)) shows that the peak in S_{eff} is a consequence of DOS band gaps where secondary band gaps (E_g) are observed in band structure. The impact of DOS on Seebeck can be qualitatively understood by expanding the Mott formula $S = (\pi^2/3)(k_B^2T/e)\partial \ln \sigma(E)/\partial E|_{E_f}$ [53]. Approximating the TDF $\sigma(E)$ from equation (5) near the Fermi level as $\sigma(E_f) \approx (e/2)v_f(\theta)^2 D(E_f)/S_o$ [42] means that $S \propto D'(E_f)/D(E_f)$, which is maximized when E_f is near a sharp discontinuity in the DOS, in this case a band edge. The gaps in DOS also reduce scattering because inelastic phonon emission from states within an energy ω_{op} the bottom of a subband is suppressed, which in-turn helps create a narrow TDF, further benefiting TE properties [18].

The simplified expression for TDF has also been widely used to estimate the twist-angle dependence of conductivity from the Fermi velocity as $\sigma(\theta) \approx$ $\sigma(0)[v_f(\theta)/v_f]^2$ [54] at low temperatures and carrier concentrations. However, the TDF also includes the temperature-dependent Fermi window $(\partial f_0/\partial E)$ whose width is $\approx 5 k_B T$ [18] so transport occurs over a range of energies around E_f , which widens the peak in S_{eff} and the minimum in σ_{eff} as functions of twist angle. This trend is illustrated by observing the S_{eff} and the corresponding σ_{eff} for different twist angles in figure 3(e). Taken together, they produce a peak in PF at room temperature at twist angles around θ = 1.3° for both electrons and holes, with maximum PF reaching around 40 mW m⁻¹ K⁻² (figure 3(d)). The peaks in PF occur at a carrier density of 3.9 \times 10^{12} cm⁻² in holes and 4.7×10^{12} cm⁻² in electrons,

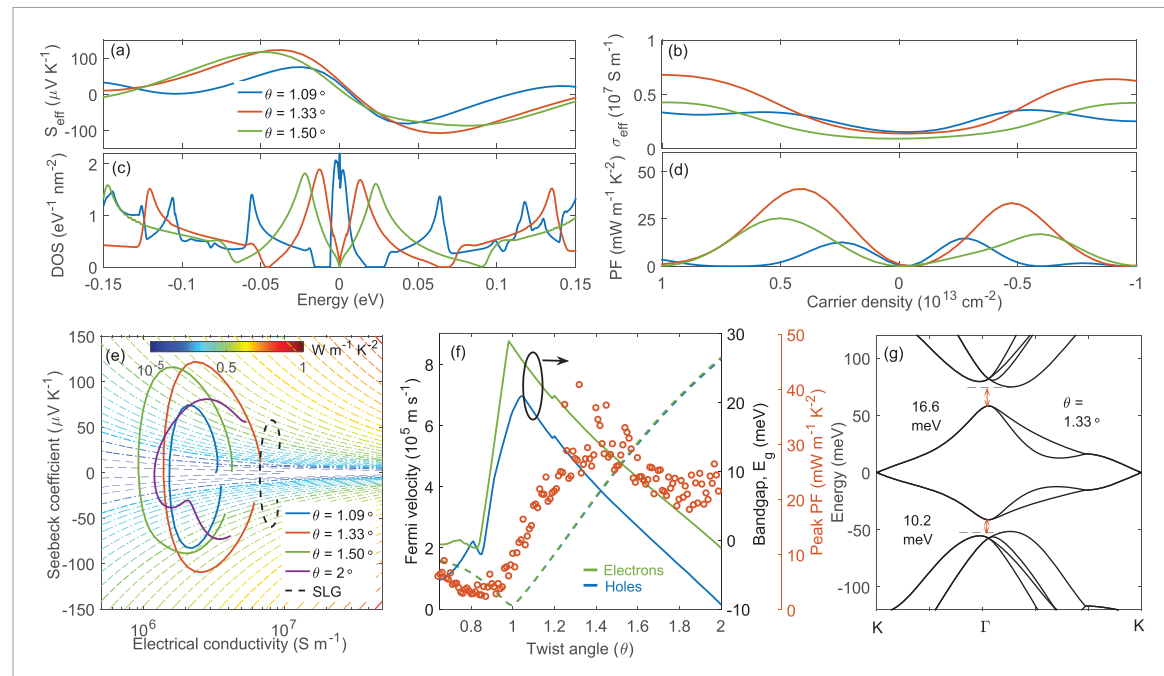


Figure 3. (a)–(d) TE properties near magic angle ($\theta=1.09^{\circ}$), at twist angle of highest PF ($\theta=1.33^{\circ}$), and at twist angle of maximum S_{eff} ($\theta=1.50^{\circ}$) (a) S_{eff} , (b) DOS, (c) σ_{eff} , and (d) PF at T=300 K. The secondary gap in the band structure results in a gap in DOS that maximizes the S_{eff} (e) Room temperature S_{eff} vs σ_{eff} of TBG at different twist angles compared with SLG to understand the PF peak at $\theta=1.28^{\circ}$. The constant PF lines are plotted as a guide to the PF. (f) Change in the carrier Fermi velocities of TBG with twist angle. The secondary bandgap (E_g) for electrons and holes at different twist angles. (g) Band structure, Fermi velocity and band gap of TBG at a twist angle $\theta=1.33^{\circ}$ where the highest PF is observed.

near complete band-filling $n_s = \pm 4.1 \times 10^{12}$ cm⁻². This stands in contrast to other notable properties of TBG, superconductivity and Mott insulating behavior, which typically occur at half-filling. The range of twist angles we simulated domain is limited to angles above 0.65° due to limitations of the continuum model that we used for band structure calculations. This limitation comes from the inclusion of atomic relaxation in TBG that suppress the secondary magic-angle below $\theta = 0.65^{\circ}$. However, the band gaps occurring at magic angles below 0.65° are smaller [55, 56], so we expect them to result in lesser enhancements of Seebeck and PF.

The impact of band gap E_g on S_{eff} is reflected in the PF, as shown by the plot of maximum PF reached either in electrons or holes at each twist angle along with the corresponding electron and hole secondary band gaps (E_g) in figure 3(f). Both electron and hole band gaps peak near the 1° twist angle due to the gaps and flat bands in the band structure. The flattening is also evident in the corresponding electron and hole Fermi velocities at different twist angles. The growing gap near magic angle is beneficial to S_{eff} as gapping suppresses bipolar transport, while the asymmetry in the DOS increases average carrier energy relative to the Fermi level. On the other hand, lower Fermi velocity is directly reflected in a decrease of conductivity, particularly at low carrier densities. Taken together, the highest PF occurs when the gain in Seebeck overtakes the loss of conductivity, indicated by the peak PF occurring when the E_g and v_F plots cross in figure 3(f). Figure 3(e) shows the band structure at a twist angle

 $\theta=1.33^{\circ}$, at which the PF peaks, along with the band gap between first and second bands, which is 16.6 meV in electrons and 10.2 meV in holes.

To understand the temperature dependence of PF in TBG, we calculated the TE properties at T =100 K and T = 200 K while changing the twist angle. Figures 4(a) and (b) shows the PF at different twist angles and carrier densities at T = 100 K and T =200 K. With decreasing temperature, the carrier concentration and the twist angle at which the PF peaks both decrease. The twist angle at which PF peaks is lowered slightly from $\theta = 1.33^{\circ}$ at 300 K to $\theta =$ 1.26° at 100 K. The maximum PF either in holes or electrons at T = 100 K and T = 200 K is compared with the values observed at room temperature in figure 4(c). A maximum PF of 80 mW $m^{-1}K^{-2}$ is observed at T = 200 K, increasing to 140 mW $m^{-1} K^{-2}$ at T = 100 K, representing increases of 51% and 100%, respectively, relative to SLG, which is plotted by the dotted black line in figure 4(c). TBG exhibits increasing PF with lowered temperature, opposite to the trend observed in SLG [5]. This reversal can be explained by the presence of the band gaps in TBG, which help suppress bipolar transport when the gap is larger than the 5 k_B T width of the Fermi window $\partial f_0/\partial E$. Similar temperature dependence has been previously observed in high- T_c superconductor FeSe [57], where the PF in ultrathin samples increased an order in magnitude from 300 to 100 K.

The observed peaks in PF coincide with the peak in bandgap between second and first bands for both

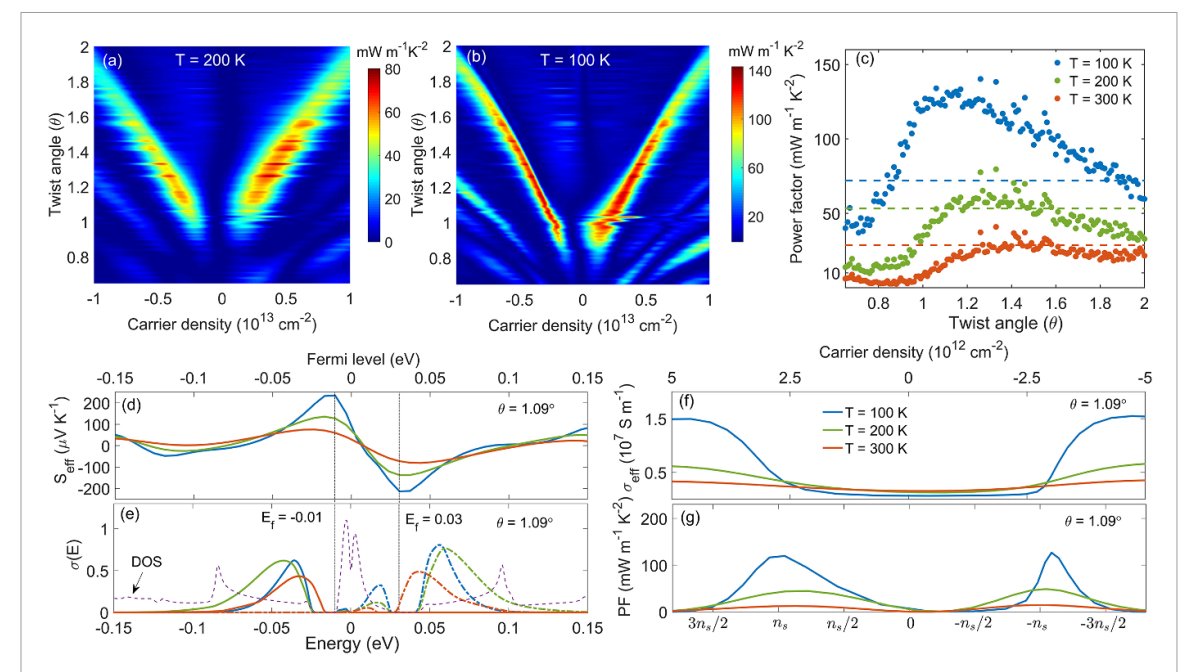


Figure 4. PF at (a) T=200 K and (b) T=100 K of TBG at different twist angles. (c) Temperature dependence of peak PF at twist angles of TBG, observed by varying the carrier densities. The peak in PF is observed at $\theta=1.33^\circ$ at T=300 K, decreasing slightly to $\theta=1.26^\circ$ for T=100 K. (d) Temperature dependence of S_{eff} at $\theta=1.09^\circ$. (e) $\sigma(E)$ at Fermi levels where peak in S_{eff} is observed at T=100 K. S_{eff} peaks when $\sigma(E)$ is asymmetric with respect to the corresponding Fermi level. Variation in (f) σ and (g) PF with temperature at $\theta=1.09^\circ$ at different carrier densities. The peak in PF is observed at a carrier densities near $\pm n_5$ depending on the temperatures.

electrons and holes (shown previously in figure 3(f)). In figure 4(d), S_{eff} is plotted near the magic angle at $\theta = 1.09^{\circ}$, while varying the carrier concentration by moving the position of the Fermi level (E_f). The Seebeck coefficient increases with asymmetry in TDF in the vicinity of E_f , which is maximized at the edge of a band. Once the lowest subband is completely filled, increasing E_f further causes carriers to fill the second subband. There the DOS flattens, causing $\sigma'(E_f)$ to decrease and eventually change sign, resulting in the reversal of the sign of S_{eff} at high carrier densities seen in figure 4(d). Contrary to SLG, S_{eff} in TBG increases with decreasing temperature, which can be explained from the TDF σ (E) shown in figure 4(e), where σ (*E*) is plotted at the carrier densities where S_{eff} is maximum for holes and electrons, which correspond to $E_f = -0.01$ and $E_f = 0.03$, respectively. The TDF shown in figure 4(e) has pronounced broad peaks above (below) the gap for electrons (holes), indicating considerable contributions transport through the remote bands flanking the gaps. Since the flat bands are below (above) the Fermi level for electrons (holes), their contribution has the opposite sign in $(E - E_f)$ so transport through them is detrimental to the Seebeck coefficient. At lower temperatures, the narrow width of the Fermi window, combined with the band gap, constrains the TDF and maximizes its slope, which increases S_{eff} . At this twist angle, σ_{eff} is also boosted at lower temperature due to the reduction in linear-in-T carrier-phonon scattering, resulting in a higher PF at low temperatures. Nonetheless,

the peak in PF vs. carrier densities remains near $\pm n_s$ at 100 and 200 K, as shown in figure 4(g).

However, the electronic structure model employed in this work does not capture Hartree effects, which have been shown to make the electronic structure sensitive to the filling level [58]. As the local density of states in the moiré superlattice is larger in the AA regions than in the AB/BA regions, additional carriers preferentially localize in the AA regions, creating a non-uniform charge distribution. The Coulomb interactions give rise to a strong Hartree potential and a filling-dependent change in the low-energy bands. For hole doping, this implies an increase of the energy of the states at the Gamma point [59], while leading to a further flattening of the flat bands for either doping [60], narrowing the bandwidth and increasing the gaps [61]. The shape and position of van Hove singularities are also impacted [62], which has been observed experimentally [63]. Recent studies have further examined the impact of Coulomb interactions on electronic structure [64, 65]. Based on our transport model, we expect that decreasing bandwidth (increasing gaps) and flattening the bands would further minimize the 'bipolar' contribution from the flat bands to transport, thereby increasing the Seebeck coefficient. On the other hand, their contribution to conductivity, which is always positive, would decrease slightly. Since the PF is increased when the Fermi window is narrower than the gap at low temperatures, we can expect that smaller bandwidth (larger gaps) would similarly have a net favorable impact on the PF, analogous to lowering the temperature.

In conclusion, we calculated phonon-limited TE transport properties of TBG for a range of twist angles, carrier densities, and at several temperatures. Both acoustic and optical phonon scattering rates were included to capture carrier-lattice interactions. Band structure of TBG is obtained from an exact continuum model coupled with tight-binding Hamiltonians, while transport is captured using an iterative solver for the Boltzmann equation. Our calculations show a peak PF of around 40 mW m⁻¹ K⁻² at room temperature, observed at a twist angle of 1.33°, which is slightly above the magic angle. The peak PF value is roughly 40% higher than the highest PF calculated in SLG. As twist angle approaches the magic angle, a gap opens in the electronic structure, which improves the Seebeck coefficient, while the Fermi velocity is lowered, depressing conductivity. The gain in the Seebeck outweighs the loss in conductivity, resulting in higher PF at angles slightly above the magic angle. As temperature is lowered, the peak PF increases as the narrower Fermi window helps suppress bipolar transport, reaching 80 and 140 mW m⁻¹ K⁻² at 200 and 100 K, respectively. We conclude that, using temperature and twist angle as knobs, TE properties of TBG can be tuned to achieve superlative performance. Owing to the increase in Seebeck coefficient relative to SLG, junctions between BLG and SLG could form highly sensitive thermocouples. These unique properties of TBG make it a promising candidate for future TE devices that can be operated under a wide spectrum of performance requirements in energy conversion and thermal sensing applications.

Data availability statement

The data that support the findings of this study are available upon reasonable request from the authors.

Acknowledgment

The authors thank Drs Efthimios Kaxiras, Jun Yan, and Stephen Carr for fruitful discussions and NSF for financial support through Award 1902352.

ORCID iD

Zlatan Aksamija https://orcid.org/0000-0001-9085-9641

References

- [1] Goldsmid H J 1964 Thermoelectric Refrigeration (New York:
- [2] Pei Y Wang H Snyder G J 2012 Band engineering of thermoelectric materials Adv. Mater. 24 6125–35
- [3] Snyder G J and Toberer E S 2008 Complex thermoelectric materials Nat. Mater. 7 105–14

- [4] Yan Y Jin Y R Zhang G Yang J Wang Y Ren W 2017 Optimum electronic structures for high thermoelectric figure of merit within several isotropic elastic scattering models Sci. Rep 7 10104
- [5] Duan J Wang X Lai X Li G Watanabe K Taniguchi T Zebarjadi M Andrei E Y 2016 High thermoelectricpower factor in graphene/hBN devices *Proc. Natl Acad. Sci.* 113 14272–6
- [6] Zebarjadi M 2015 Electronic cooling using thermoelectric devices Appl. Phys. Lett. 106 203506
- [7] Harzheim A Könemann F Gotsmann B van der Zant H Gehring P 2020 Single-material graphene thermocouples Adv. Funct. Mater. 30 2000574
- [8] Cao Y Fatemi V Fang S Watanabe K Taniguchi T Kaxiras E Jarillo-Herrero P 2018 Unconventional superconductivity in magic-angle graphene superlattices Nature 556 43–50
- [9] Cao Y et al 2018 Correlated insulator behaviour at half-filling in magic-angle graphene superlattices Nature 556 80–4
- [10] Bistritzer R and MacDonald A H 2011 Moiré bands in twisted double-layer graphene Proc. Natl Acad. Sci 108 12233–7
- [11] MacDonald A H and Bistritzer R 2011 Graphene moiré mystery solved? Nature 474 453–4
- [12] Lisi S et al 2021 Observation of flat bands in twisted bilayer graphene Nat. Phys. 17 189–93
- [13] Balents L Dean C R Efetov D K Young A F 2020 Superconductivity and strong correlations in Moiré flat bands Nat. Phys. 16 725–33
- [14] Lu X et al 2019 Superconductors, orbital magnets and correlated states in magic-angle bilayer graphene Nature 574 653–7
- [15] Li G Luican A Lopes dos Santos J M B Castro Neto A H Reina A Kong J Andrei E Y 2010 Observation of Van Hove singularities in twisted graphene layers *Nat. Phys.* 6 109–13
- [16] Kommini A and Aksamija Z 2016 Low-temperature enhancement of the thermoelectric Seebeck coefficient in gated 2D semiconductor nanomembranes *J. Comput. Electron.* 15 27–33
- [17] Mahan G D 1989 Figure of merit for thermoelectrics J. Appl. Phys. 65 1578–83
- [18] Kommini A and Aksamija Z 2019 Materials selection rules for optimum power factor in two-dimensional thermoelectrics J. Phys.: Mater. 3 015005
- [19] Mahapatra P S Sarkar K Krishnamurthy H R Mukerjee S Ghosh A 2017 Seebeck coefficient of a single van der Waals junction in twisted bilayer graphene *Nano Lett.* 17 6822–7 (PMID: 28841026)
- [20] Mahapatra P S Ghawri B Garg M Mandal S Watanabe K Taniguchi T Jain M Mukerjee S Ghosh A 2020 Misorientation-controlled cross-plane thermoelectricity in twisted bilayer graphene *Phys. Rev. Lett.* 125 226802
- [21] Kubakaddi S S 2020 Giant thermopower and power factor in twisted bilayer graphene at low temperature *J. Phys.: Condens. Matter.* 33 245704
- [22] Kommini A and Aksamija Z 2018 Thermoelectric properties of periodic quantum structures in the Wigner-Rode formalism J. Phys.: Condens. Matter 30 044004
- [23] Kommini A and Aksamija Z 2020 Anisotropic thermoelectric power factor of two-dimensional materials with periodic potential barriers: the Wigner-Rode formalism *Phys. Rev. Appl.* 14 034037
- [24] Rode D L 1971 Electron Transport in InSb, InAs and InP Phys. Rev. B 3 3287
- [25] Zuev Y M Chang W Thermoelectric K, P and 2009 Magnetothermoelectric transport measurements of graphene Phys. Rev. Lett. 102 096807
- [26] Marel D v d *et al* 2003 Quantum critical behaviour in a high-Tc superconductor *Nature* 425 271—4
- [27] Cao Y Chowdhury D Rodan-Legrain D Rubies-Bigorda O Watanabe K Taniguchi T Senthil T Strange J-H, P 2020 Metal in magic-angle graphene with near Planckian dissipation *Phys. Rev. Lett.* 124 076801

- [28] Emery V J and Kivelson S A 1995 Superconductivity in bad metals Phys. Rev. Lett. 74 3253–6
- [29] Bruin J A N Sakai H Perry R S Mackenzie A P 2013 Similarity of scattering rates in metals showing T-linear resistivity Science 339 804–7
- [30] Polshyn H, Yankowitz M, Chen S, Zhang Y, Watanabe K, Taniguchi T, Dean C R and Young A F 2019 Large linear-intemperature resistivity in twisted bilayer graphene *Nat. Phys.* 15 1011–6
- [31] Wu F MacDonald A H Martin I 2018 Theory of phonon-mediated superconductivity in twisted bilayer graphene Phys. Rev. Lett. 121 257001
- [32] Yudhistira I Chakraborty N Sharma G Ho D Y H Laksono E Sushkov O P Vignale G Adam S 2019 Gauge-phonon dominated resistivity in twisted bilayer graphene near magic angle Phys. Rev. B 99 140302
- [33] Hwang E H and Das Sarma S 2008 Acoustic phonon scattering limited carrier mobility in two-dimensional extrinsic graphene Phys. Rev. B 77 115449
- [34] Zarenia M Yudhistira I Adam S Vignale G 2020 Enhanced hydrodynamic transport in near magic angle twisted bilayer graphene Phys. Rev. B 101 045421
- [35] Kubakaddi S S and Bhargavi K S 2010 Enhancement of phonon-drag thermopower in bilayer graphene *Phys. Rev.* B 82 155410
- [36] Correa G C Foss C J Aksamija Z 2017 Interface thermal conductance of van der Waals monolayers on amorphous substrates *Nanotechnology* 28 135402
- [37] Yasaei P *et al* 2015 Scattering in graphene grain boundaries *Nano Lett.* **15** 4532–40
- [38] Borysenko K M Mullen J T Barry E A Paul S Semenov Y G Zavada J M Nardelli M B Kim K W 2010 First-principles analysis of electron-phonon interactions in graphene *Phys. Rev.* B 81 121412
- [39] Kanahashi K Ishihara M Hasegawa M Ohta H Takenobu T 2019 Giant power factors in p- and n-type large-area graphene films on a flexible plastic substrate npj 2D Mater. Appl. 3 44
- [40] Cocemasov A I Nika D L Balandin A A 2013 Phonons in twisted bilayer graphene Phys. Rev. B 88 035428
- [41] Duan J Wang X Lai X Li G Watanabe K Taniguchi T Zebarjadi M Andrei E Y 2016 High thermoelectricpower factor in graphene/hBN devices *Proc. Natl Acad. Sci. USA* 113 14272–6
- [42] Hwang E H Rossi E Das Sarma S 2009 Theory of thermopower in two-dimensional graphene *Phys. Rev.* B 80 235415
- [43] Ghahari F Xie H-Y Taniguchi T Watanabe K Foster M S Kim P 2016 Enhanced thermoelectric power in graphene: violation of the Mott relation by inelastic scattering *Phys. Rev. Lett.* 116 136802
- [44] Carr S Fang S Zhu Z Kaxiras E 2019 Exact continuum model for low-energy electronic states of twisted bilayer graphene *Phys. Rev. Res.* 1 013001
- [45] Fang S, Carr S, Zhu Z, Massatt D and Kaxiras E 2019 Angle-dependent ab initio low-energy Hamiltonians for a relaxed twisted bilayer graphene heterostructure (arXiv:1908.00058)
- [46] Cao Y et al 2018 Correlated insulator behaviour at half-filling in magic-angle graphene superlattices Nature 556 80–4

- [47] Kim K Mason B A Hess K 1987 Inclusion of collision broadening in semiconductor electron-transport simulations *Phys. Rev.* B 36 6547–50
- [48] Reggiani L Lugli P Jauho A P 1987 Quantum kinetic equation for electronic transport in nondegenerate semiconductors Phys. Rev. B 36 6602–8
- [49] Aksamija Z and Ravaioli U 2009 Energy conservation in collision broadening over a sequence of scattering events in semiclassical Monte Carlo simulation J. Appl. Phys. 105 083722
- [50] Pletikosić I Kralj M Milun M Pervan P 2012 Finding the bare band: electron coupling to two phonon modes in potassium-doped graphene on Ir(111) Phys. Rev. B 85 155447
- [51] Borysenko K M Mullen J T Li X Semenov Y G Zavada J M Nardelli M B Kim K W 2011 Electron-phonon interactions in bilayer graphene Phys. Rev. B 83 161402
- [52] Koshino M and Nam N N T 2020 Effective continuum model for relaxed twisted bilayer graphene and Moiré electron-phonon interaction *Phys. Rev.* B 101 195425
- [53] Jonson M and Mahan G D 1980 Mott's formula for the thermopower and the Wiedemann-Franz law Phys. Rev. B 21 4223
- [54] Das Sarma S and Wu F 2020 Electron-phonon and electron-electron interaction effects in twisted bilayer graphene Ann. Phys. 417 168193
- [55] Tarnopolsky G Kruchkov A J Vishwanath A 2019 Origin of magic angles in twisted bilayer graphene *Phys. Rev. Lett.* 122 106405
- [56] Song Z Wang Z Shi W Li G Fang C Bernevig B A 2019 All magic angles in twisted bilayer graphene are topological Phys. Rev. Lett. 123 036401
- [57] Shimizu S Shiogai J Takemori N Sakai S Ikeda H Arita R Nojima T Tsukazaki A Iwasa Y 2019 Giant thermoelectric power factor in ultrathin FeSe superconductor *Nat. Commun.* 10 825
- [58] Guinea F and Walet N R 2018 Electrostatic effects, band distortions and superconductivity in twisted graphene bilayers Proc. Natl Acad. Sci. USA 115 13174–9
- [59] Rademaker L Abanin D A Mellado P 2019 Charge smoothening and band flattening due to Hartree corrections in twisted bilayer graphene Phys. Rev. B 100 205114
- [60] Goodwin Z A H Vitale V Liang X Mostofi A A Lischner J 2020 Hartree theory calculations of quasiparticle properties in twisted bilayer graphene Electron. Struct. 2 034001
- [61] Calderón M J and Bascones E 2020 Interactions in the 8-orbital model for twisted bilayer graphene Phys. Rev. B 102 155149
- [62] Cea T Walet N R Guinea F 2019 Electronic band structure and pinning of Fermi energy to Van Hove singularities in twisted bilayer graphene: a self-consistent approach *Phys. Rev.* B 100 205113
- [63] Kerelsky A *et al* 2019 Maximized electron interactions at the magic angle in twisted bilayer graphene *Nature* **572** 95–100
- [64] Vafek O and Kang J 2020 Renormalization group study of hidden symmetry in twisted bilayer graphene with coulomb interactions Phys. Rev. Lett. 125 257602
- [65] Bernevig B A Song Z-D Regnault N Lian B 2021 Twisted bilayer graphene. I. Matrix elements, approximations, perturbation theory and a k · p two-band model Phys. Rev. B 103 205411